Intrinsic fluorescence in non-aromatic peptide structures is induced by collective vibrations, charge reorganisation and short hydrogen bonds, as shown in a new glutamine-related structure

Amberley D. Stephens,*[1] Muhammad Nawaz Qaisrani,*[2,3] Michael T. Ruggiero,[4,1] Saul T.E. Jones,[5] Emiliano Poli,[2] Andrew D. Bond,[6] Philippa J. Woodhams,[1] Elyse M. Kleist,[7] Luca Grisanti,[8] Ralph Gebauer,[2] J. Axel Zeitler,[1] Dan Credgington,[5] Ali Hassanali,[2#] Gabriele S. Kaminski Schierle[1#]

[1] Chemical Engineering and Biotechnology, University of Cambridge, Cambridge CB3 0AS, UK
[2] The Abdus Salam International Centre for Theoretical Physics, Strada Costiera 11, 34151 Trieste, Italy
[3] International School for Advanced Studies, Via Bonomea 265, 34136 Trieste, Italy
[4] Department of Chemistry, University of Vermont, 82 University Place, Burlington, VT, 05405 USA
[5] Cavendish Laboratory, University of Cambridge, JJ Thomson Avenue, Cambridge, CB3 0HE, U.K
[6] Department of Chemistry, University of Cambridge, Lensfield Road, Cambridge CB2 1EW, United Kingdom
[7] Department of Chemistry, Syracuse University, Syracuse, New York 13244, United States
[8] Division of Theoretical Physics, Ru¯der Boškovi´c Institute, Bijeni˘cka cesta 54, 10000 Zagreb, Croatia
* Contributed equally
[#] Corresponding authors: ahassana@ictp.it, gsk20@cam.ac.uk

Abstract

Disentangling the origin of the optical activity of non-aromatic proteins is challenging due to their size and thus their high computational requisites. Here we show, in a much smaller model system, that the single amino acid glutamine undergoes a chemical transformation leading to an unreported glutamine-like structure which has a similar broad absorption spectrum reported previously for non-aromatic proteins. We further show computationally that the optical activity of the glutamine-like structure is directly coupled to short-hydrogen bonds, but also displays charge and vibrational fluctuations, the latter of which are also present in less optically active structures such as in L-glutamine. Since experimentally the glutamine-like structure is the brightest structure, we conclude that short-hydrogen bonds are the ones responsible for the large Stokes shift observed in optically active non-aromatic proteins.

Introduction

Short peptides void of any aromatic residues have been shown to display an intrinsic fluorescence in the visible range (*1*, *2*). This has primarily been observed in fibrillar protein structures linked to neurodegenerative diseases, such as Alzheimer's, Parkinson's and Huntington's diseases (*3*–*6*). Furthermore, optical properties of double amino acid based nanowires have also been reported, existing either of two non-aromatic or two aromatic amino acids (*2*, *7*, *8*). We have shown that the fluorescence of non-aromatic short crystal structures forming part of the amyloid-beta protein is enhanced by the presence of short hydrogen bonds (SHB) between the termini of prefibrillar structures (*5*). The SHB permits proton transfer leading to a double-well ground state potential which we have proposed prevents a conical intersection in the excited state (*5*). It has been suggested that one of the prerequisites for this fluorescence observed in either amyloid structures or short peptide nanowires is related to hydrogen bonding or aromatic interlocks which, for the latter, decreases the bandgaps down to the semiconductive regions (*9*).

Despite our previous suggestion that proton delocalisation is strongly coupled to this intrinsic fluorescence, its direct role and more importantly, the role of other vibrational modes on putative fluorescing states, has not been elucidated. We have thus searched for a model system, such as a single amino acid-based structure, that displays similar optical properties to amyloid fibrils and is permissive to more sophisticated computational approaches. We have been inspired by the small peptide nanostructures that have been pioneered by the Gazit laboratory (*9*) and by the fact that there are several neurodegenerative diseases that have been connected with an increased level of glutamines produced as part of a protein, as for example Huntingtin in Huntington's disease which renders the protein more aggregation prone (*10*). It has been known that the amide group in L-glutamine (L-glu) is highly labile and thus can rapidly hydrolyse. We show here that the single amino acid L-glu upon heating in water can form a nanostructural material with optical properties similar to the ones observed in other amyloid fibrils such as in fibrils of amyloid-beta, alpha-synuclein or tau (*4*, *11*, *12*).

Using X-ray diffraction (XRD), we show that L-glu dissolved in water and upon heating becomes cyclysed forming a previously unreported structure which resembles L-pyroglutamine (which has been reported to be a component of amyloid-beta in the brain (*13*)), but involves a low-barrier hydrogen bonded anionic dimer with an ammonium counterion. We have termed the new structure, i.e. L-pyroglutamine complexed with an ammonium ion, L-pyro-amm. L-pyro-amm has a microcrystalline plate morphology as shown by scanning electron microscopy (SEM). The newly formed solid was further characterised using terahertz time-domain spectroscopy (THz-TDS), which provides information on the low-frequency modes in the crystal that control the proton transfer. Additionally, the experiments were interpreted using ground and excited state electronic structure calculations and molecular dynamics simulations. Ultimately, the combination of static structural information, atomic vibrational dynamics, and optical properties enable the origins of fluorescence in this particular structure to be elucidated, shedding light on the complementary processes in more complex systems.

Methods

Experimental

Sample preparation of L-glutamine

L-glutamine (L-glu) (#G3126, #G8540, Sigma-Aldrich, Gillingham, UK) and L-pyroglutamine (L-pyro) (#83160, Sigma-Aldrich) were dissolved in 18.2Ω MilliQ H_2O at a concentration of 0.3 M or 1 M. Aliquots were placed in a 65°C oven, since heating up proteins to 65°C increases the formation of amyloid structures as reported previously (*14*). Each aliquot was rotated to dissolve the powder once a day. Samples were either analysed in liquid form or dried on a glass or quartz cover slip (#043210.KG, Alfa Aesar, Lancashire, UK) either at room temperature (RT) or on a heat block set to 50°C.

Emission and excitation wavelength scans

Emission and excitation spectra were taken on a Hitachi F-4500 FL spectrophotometer (Hitachi High-Technologies Corporation, Tokyo, Japan) at RT in a quartz cuvette. For measurements, the excitation slit resolution was 5 nm or 10 nm and the emission slit resolution was 20 nm. The PMT voltage was set at 950 V and the scan speed set at 240

101 nm/min. The excitation scan was measured between 250 – 400 nm and the emission filter
102 set to the emission maxima of the sample stated in the figure legend, with a slit resolution
103 of 20 nm. The emission scan was measured between 380 - 560 nm and the excitation filter
104 set to the excitation maxima of the sample stated in the figure legend, using a slit resolution
105 of 5 nm. Four measurements were taken for each sample which was repeated at least three
106 times and the background (air or H_2O) was subtracted from the average.
107
108 *Absorption measurements*
109 Absorption measurements were taken on a UV-Vis-NIR Spectrophotometer, UV-3600 Plus
110 (Shimadzu, Kyoto, Japan) and Cary 6000i (Agilent, Santa Clara, USA). 1 M or 0.3 M L-glu, L-
111 pyro or L-pyro-amm solutions were measured in 10 mm QX cuvettes (Hellma Analytics,
112 Müllheim, Germany) or dried on quartz coverslips. Measurements were taken between
113 wavelengths 200 – 800 nm using 1 nm steps at a slow scan speed and a 1 nm resolution. The
114 light source change wavelength was set at 393 nm and the grating change wavelength set at
115 750 nm. Samples were measured at least three times and the experiments repeated at least
116 three times, measurements were then averaged and H_2O or coverslip only control was
117 subtracted.
118
119 *SEM (scanning electron microscopy)*
120 SEM was performed using a FEI Magellan 400 HR-SEM at an acceleration voltage of 2 kV. L-
121 pyro-amm samples were lyophilised by freezing in liquid nitrogen and freeze drying in a
122 LyoQuest 85 (Telstar, Terrassa, Spain) and imaged on a glass coverslip.
123
124 *X-ray diffraction*
125 L-pyro-amm was dried on a glass coverslip in a 50°C oven and then at RT until crystals
126 formed. Single crystal X-ray diffraction (SCXRD) measurements were performed at 180 K
127 with a Bruker D8-QUEST PHOTON-100 diffractometer, which utilised a Cu Kα radiation (λ =
128 1.54 Å), and an APEX-II CCD. Absorption corrections were made using SDABS, and data
129 integration and reduction were performed with SAINT+. All non-hydrogen atoms were
130 refined isotropically and anisotropically, followed by inclusion of the hydrogen atoms
131 (determined using the excess electron density) and refinement isotropically.
132

133 *Terahertz Time-Domain Spectroscopy*

134 All THz-TDS spectra were acquired using a commercial Terapulse 4000 spectrometer
135 (TeraView Ltd, Cambridge, UK). Samples were prepared for THz-TDS measurements by
136 diluting the solid air dried L-pyro-amm with polyethylene (~ 10% w/w concentration) by
137 gentle mixing using an agate mortar, followed by pressing into 2 mm thick, 13 mm diameter
138 pellets using a hydraulic press. All THz-TDS spectra shown are a result of division of sample
139 and blank datasets, with the blank dataset represented the THz-TDS response of a pellet of
140 pure polyethylene.

141

142 *Theoretical*

143 *DFT-THz Calculations*

144 Calculations were performed using both the CRYSTAL17 (*15*) and Quantum Espresso (*16*)
145 software packages. Geometry optimisations and vibrational analyses performed with the
146 CRYSTAL17 code utilised the atom-centred split-valence triple-zeta 6-311g(2d,2p) basis set
147 for all atom types. Based on a previous study related to ionic molecular crystals (*17*), the
148 range-corrected WB97-X (*18*) functional was used. The vibrational analysis was performed
149 within harmonic approximation, and infrared intensities were determined using the Berry
150 Phase method. Energy convergence criteria were set to $\Delta E < 10^{-8}$ and 10^{-11} hartree for the
151 geometry and frequency calculations, respectively.

152

153 *Periodic TD-DFT Excited State Calculations*

154 Simulations were performed using the fully periodic Quantum Espresso software package.
155 The Becke-Lee-Yang-Parr (B3LYP) hybrid density functional was used with an energy cutoff
156 of 40 Ry. The calculations of the excited state were performed within the framework of
157 TDDFT using the Liouville-Lanczos formalism implemented in the freely available Quantum-
158 Espresso package (*19*). In this approach, the optical spectra are obtained directly over the
159 wide spectral range without taking into account the numerically complex calculations of the
160 single exited states. We used plane wave basis set and the electron-ion interactions were
161 taken into account via norm conserving Martins-Troullier pseudopotentials (*20*). To
162 determine the ground state wave function, we used the gamma point of the Brillouin zone.
163 All the periodic calculations employed the computationally demanding B3LYP (*21*) hybrid

164 functional, the kinetic energy cutoff of 40 Ry was used for the wave functions. The intrinsic
165 band width for the spectra was set to 0.003 Ry (~0.0408 eV).
166
167 *Periodic Structure Geometry Optimisation*
168 The structures obtained from the experiments were first geometrically optimized at 0°K
169 using the Broyden-Fletcher-Goldfarb-Shanno (BFGS) minimisation algorithm implemented in
170 CP2K (*22*, *23*) package. A convergence criterion for the wave function optimisation was used
171 as $5x10^{-7}$ a.u. Applying the method of the Gaussian and plane wave, the wave function was
172 expended in the Gaussian double-zeta valence polarised (DZVP) basis set. The cutoff for the
173 electronic density was set to 300 Ry. We used the gradient correction to the local density
174 approximation and the core electrons were treated via Goedecker-Teter-Hutter
175 pseudopotentials (*24*). In all the calculations, we used the Becke-Lee-Yang-Parr (BLYP) (*25*)
176 functional with the D3(0) Grimme (*26*) dispersion corrections for the van der Waals
177 interactions.
178
179 *Ab Initio Molecular Dynamics Simulations*
180 Ab initio Molecular Dynamics simulations (AIMD) were performed using Quickstep
181 algorithm implemented in CP2K. In these calculations, the propagation of the nuclei was
182 taken into account within the framework of the Born-Oppenheimer approximation. The
183 simulations were performed in the NVT ensemble and the temperature was controlled
184 during the simulations by using the velocity-rescaling thermostat (*27*). We used the time
185 step of 0.5 femtosecond to update the nuclear coordinates and velocities while the total
186 length of the simulations for each system is 50 picoseconds.
187
188 *Excited State Cluster Calculations*
189 A set of excited state calculations were performed on glutamine clusters in order to
190 understand the role of the environment on the optical properties. Specifically, the optical
191 properties of L-pyro-amm were investigated using various isolated cluster models with the
192 Gaussian09 software package. The clusters were extracted directly from the crystal
193 structure and used in various combinations (dimers, trimers, tetramers) to perform time-
194 dependent DFT (TD-DFT) calculations. A split-valence triple-zeta 6-311g(2d,2p) basis set was
195 used for all atom types together with the hybrid B3LYP functional. Some benchmark

196 simulations, comparing the optical properties obtained from the periodic calculations using
197 B3LYP to range corrected hybrid functionals like CAM-B3LYP, were also performed with
198 these clusters.
199
200 We also performed a series of excited state optimisations on various model systems built
201 from L-pyro-amm in order to examine the nature of the geometrical distortions that occur
202 on the lowest electronic excited state. These calculations were also performed with the
203 Gaussian09 software package. All clusters were surrounded with a continuum dielectric
204 constant of 80, representing pure H_2O. The 6-311G(2d,2p) basis set was used for all atoms
205 together with the range corrected hybrid functional CAM-B3LYP (*28*). The clusters were first
206 optimised in the ground state after which they were optimised on the first electronic
207 excited state.
208
209 **Results and Discussion**
210
211 It has long been known that poly-glutamine can form amyloid-like fibrillar structures *in vitro*.
212 The more glutamine residues in the poly-glutamine polymer, the faster the aggregation
213 propensity of the polypeptide chain. This led us to investigate whether L-glu on its own
214 under conditions which normally promote fibril formation, such as an increase in
215 temperature (*14*), was able to form structures with similar optical properties, as recently
216 observed for amyloid fibrils (*5*, *29*, *30*).
217
218 We first investigated the structure of L-pyro-amm, which formed after incubation of L-glu
219 for 8 days at 65°C, using SEM and observed crystal structures shown in Fig.1a. However, in
220 order to investigate whether L-glu had indeed changed its crystal structure arrangement we
221 performed XRD analysis of the resulting material. In Fig.1b we show the crystal structure of
222 the heated L-glu structure, which we termed L-pyro-amm, and the published crystal
223 structures of L-glu and L-pyroglutamine (L-pyro) in Fig. 1c and d. Note, the L-pyro structure
224 was analysed as it displayed structural similarities to the newly formed L-pyro-amm. Figures
225 were obtained from geometry optimisations of the nuclear positions of the atoms using
226 experimental densities. L-pyro-amm consists of 8 pyroglutamine groups and 4 ammonium
227 ions (144 atoms) complexed within the crystal (see Fig. 1b). In contrast, as shown in Fig. 1c,

228 L-glu consists of 4 glutamine molecules (80 atoms) in the unit cell which form hydrogen
229 bonds involving the termini and side chain. Furthermore, as shown in Fig. 1d, L-pyro consists
230 of 12 pyroglutamine molecules (192 atoms) in the unit cell forming hydrogen bonds
231 involving the NH and COOH groups.
232
233 L-pyro-amm has a rather unique hydrogen bond network structure since four of the
234 pyroglutamine molecules are deprotonated and hence have a nominal negative charge,
235 while the other four molecules are neutral. One of the important implications of this
236 difference is that L-pyro-amm contains a very strong hydrogen bond. The red circled region
237 in Fig. 1a corresponds to a short hydrogen bond (SHB) with a length of 2.45 Å, while those in
238 L-glu and L-pyro range between ~2.55-2.85 Å.
239
240 The structural change was further confirmed using THz-TDS measurements, as this
241 technique is strongly dependent on the bulk packing arrangement (as well as on the internal
242 covalent structure) of the molecules (*31*). The THz-TDS spectrum of the resulting solid, as
243 well as the solid-state DFT predicted spectrum based on the single crystal XRD (SCXRD)-
244 determined structure, is shown in Fig. 1e (full spectral assignment available in Suppl. Fig. 1).
245 The agreement between the experimental and theoretical spectra further supports that full
246 conversion of the sample occurs and thus enables additional investigations into the
247 structural and electronic properties of the material.

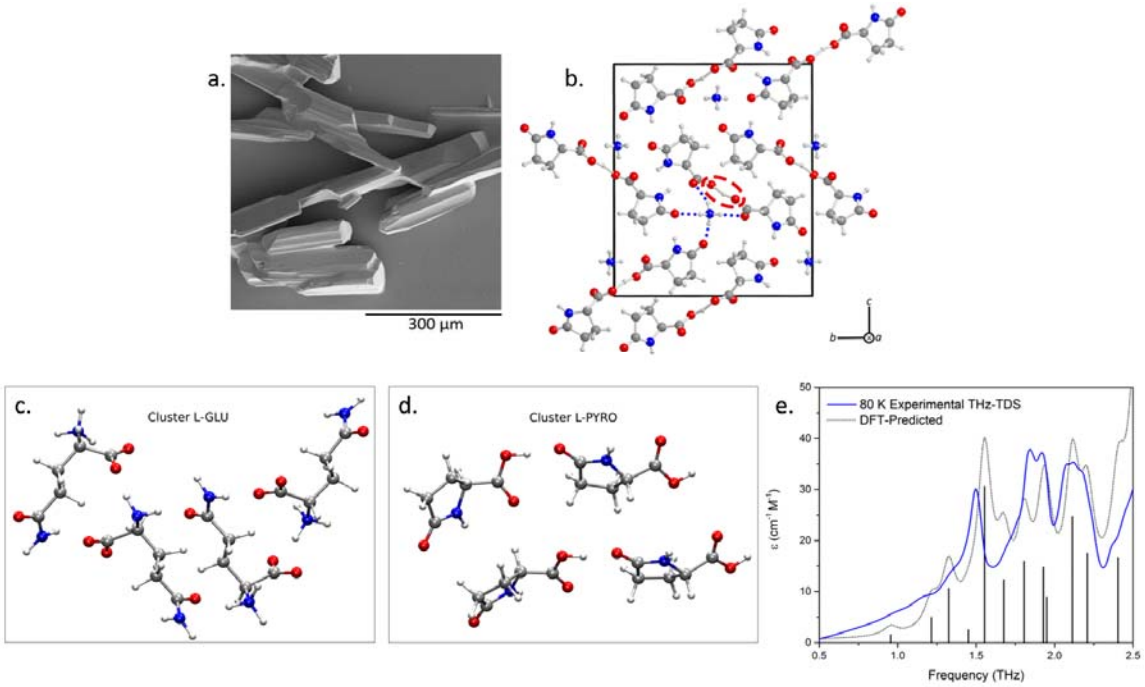

Figure 1. L-glu forms L-pyro-amm upon heating.

(a) SEM image of crystals of L-pyro-amm dried. (b) XRD analysis of heated L-glu sample show the newly formed structure, L-pyro-amm. Geometry optimisations show that 8 pyroglutamine groups and four ammonium ions (144 atoms) are complexed in the crystal and a SHB of 2.45 Å (within red dashed lines) is present near the ammonium ion (linked by bonds highlighted by blue dotted lines) (white-hydrogen, red-oxygen, blue-nitrogen, grey-carbon). (c) Clusters of L-glutamine and (d) L-pyroglutamine. (e) Experimental (blue line) and theoretical (grey line) THz-TDS of the L-pyro-amm sample are in agreement and confirm the presence of the new L-pyro-amm structure.

We first investigated whether there were any differences in the optical properties associated with the three crystal structures. Comparing the absorption of L-glu, L-pyro and L-pyro-amm in water, we show that only L-pyro-amm has a significantly red-shifted absorption which lies in the 275-320 nm range, whereas both L-glu and L-pyro primarily absorb in the deep UV (<250 nm) (see Fig. 2a).

We next compared the experimental absorption spectra of L-glu, L-pyro and L-pyro-amm with the ones obtained from time dependent density functional theory (TDDFT). We highlight here, that the small size of the systems permitted us to determine the spectra

using a hybrid functional, thereby not only advancing the quality of our theoretical predictions from previous studies (*5*, *29*, *30*) but also coupling the optical properties directly to different vibrational modes.

Fig. 2b illustrates the absorption spectra obtained for the TDDFT calculations on the 3 periodic systems in the ground state (i.e. at 0 K). Panel b.i) shows the relative oscillator strength as a function of the frequency while panel b.ii) illustrates the second derivative of the oscillator strength permitting the positions of the maxima in the spectra to be more easily identified. The spectra reveal some striking differences between the different systems. Interestingly, we observe that L-pyro is essentially dark throughout the frequency range up to ~ 6eV. On the other hand, L-pyro-amm shows the presence of more structure in the spectrum. Specifically, it is the only system for which the spectrum features a low energy excitation at 226 nm (5.5 eV) and subsequently other peaks slightly above 220 nm (5.625eV) and 216 nm (5.75eV). While L-glu exhibits a peak at 222 nm (5.58eV), it is dark up to 206 nm (~6eV). These calculations were performed with the B3LYP functional. Importantly, we have found that upon using more accurate functionals such as CAM-B3LYP (*28*) and WB97-X (*18*) L-pyro-amm remains the most optically active.

We have previously shown that thermal fluctuations and in particular nuclear vibrations, such as proton transfer, have a large impact on the absorption spectra of peptide structures compared to absorption spectra at 0 K (*5*, *32*–*34*). In Fig. 2c we show that, compared to the 0 K spectra in Fig. 2b, thermal fluctuations cause a large red shift to around 3.4 eV (365 nm) for L-pyro-amm, close to what is observed experimentally. These spectra were computed averaging over 25 frames sampled from the molecular dynamics simulations. Interestingly, no such effect is observed for L-glu which remains weakly absorbing up to more than 5 eV (247 nm) as seen at 0 K.

Similar to our previous studies on the intrinsic fluorescence of amyloid-beta fibrils, absorption is significantly increased in structures containing SHB, as neither L-glu, nor L-pyro display a significantly red shifted absorption. In order to understand better the physical origin of the low energy excitation at 226 nm (~5.5 eV) in L-pyro-amm, we computed the

electron response density at this frequency. This is illustrated in Fig. 2d, where we observe that most of the electron response involves regions around the pyroglutamine rings as well as regions near the SHB (see dashed circle in Fig. 2d). The optical response thus involves a collective charge reorganisation involving several parts of the molecular crystal.

We next investigated whether the above structures also display fluorescence excitation and emission properties as has been observed for amyloid-like structures reported previously (*5*, *29*, *30*). Fig. 2e shows the excitation scan from 250-400 nm (solid lines) with the emission set at 430 nm of L-glu in water at day 0 to 8 after incubation at 65°C. Interestingly, we observe an excitation peak at around 360 nm which is similar to what we have measured previously for amyloid proteins (*5*). The corresponding emission scan (dashed lines) with the excitation set at 360 nm and emission from 380-560 nm showed an emission peak around 430 nm, again lying in the same visible range as for amyloid fibrils. When the L-pyro-amm solution was dried the excitation and emission peaks were slightly blue shifted (Suppl. Fig. 2a) which may be due to a change in the molecular environment in the dried state. Importantly, we do not see any fluorescence in L-glu (without heating, i.e. at day 0 Fig. 2e.). To determine the importance of the ammonium ion experimentally, L-pyro has been incubated in water and heated at 65°C for 8 days, and only a very weak fluorescence has been detected (Suppl. Fig. 2b).

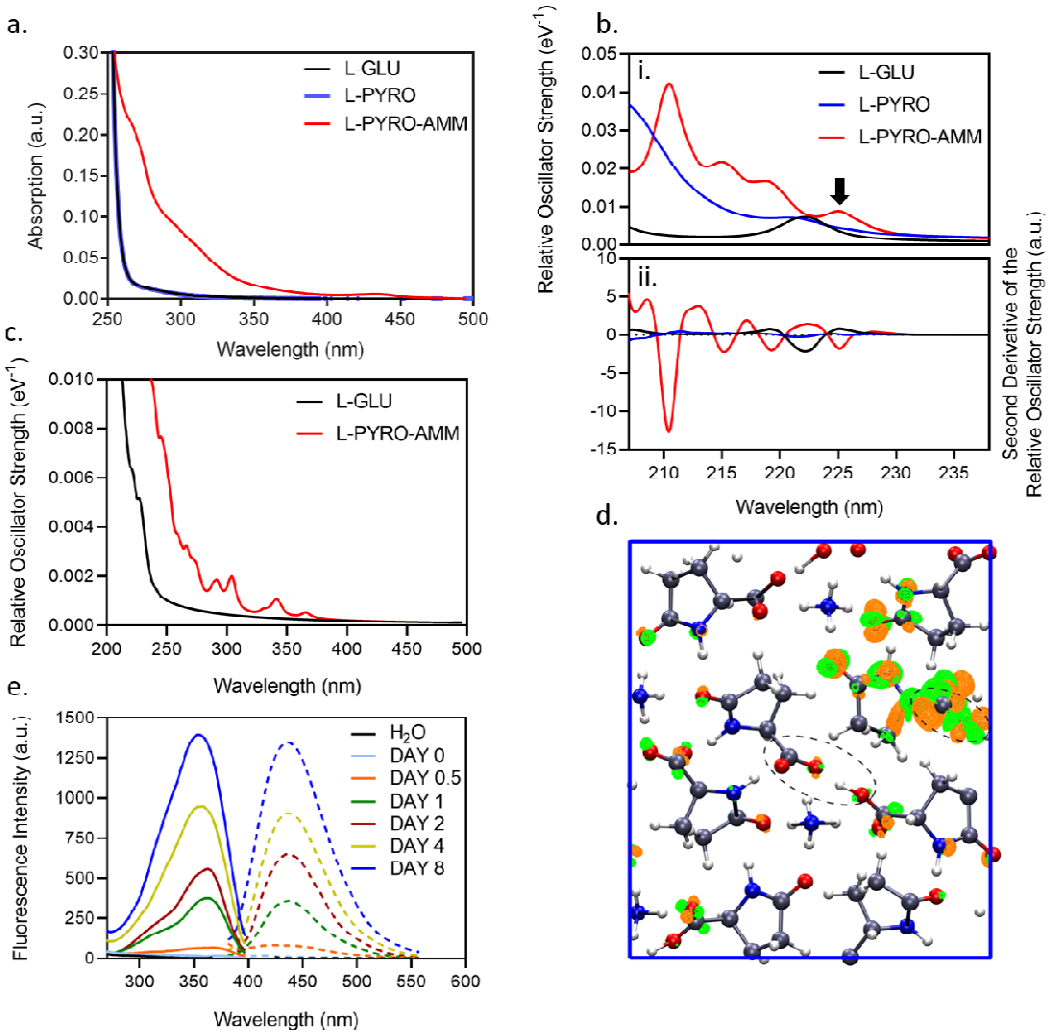

Figure 2. Optical properties of L-pyro-amm are distinct from L-glu and L-pyro

(a) Absorption spectra of 0.3 M L-glu (black), L-pyro (blue) and L-pyro-amm (red) (L-glu incubated for 8 days at 65°C) in water taken between 200 – 500 nm shows primarily features of L-pyro-amm. (b) Absorption spectra of L-glu, L-pyro and L-pyro-amm obtained from periodic density functional theory calculations with the B3LYP functional. L-pyro-amm features the lowest lying excited states which are characterised by the largest oscillator strengths. (c) Absorption spectra for L-glu and L-pyro-amm obtained from periodic simulations at room temperature. The spectra were computed by averaging over 25 frames randomly sampled from the *ab initio* molecular dynamics simulations. (d) The excited state electron density computed for L-pyro-amm from the optimised structure computed at the first peak (arrow in panel b). The lowest excited state density shows a response from various parts of the crystal structure including the pyroglutamic acid ring and the SHB region (see

331 dashed circle). The orange and green surfaces correspond to regions involving a decrease
332 and increase in electron density respectively, shown at an iso-value of $1x10^{-5}$. (e) 1 M L-glu
333 was incubated at 65°C and the excitation and emission spectra were measured over time.
334 Excitation spectra were measured between 250-400 nm with emission set at 420 nm and
335 emission spectra were measured between 380-560 nm with the excitation set at 360 nm.
336
337 It is not possible to directly pinpoint the exact mechanisms and origins of the difference in
338 the optical properties between the three systems from the ground state calculations at 0 K.
339 As alluded to earlier, one of the factors that distinguishes L-pyro-amm from the other
340 systems is the presence of the SHB (highlighted by red circles in Fig. 1a) and the presence of
341 the ammonium ion. In order to characterise the behaviour of the SHB, we conducted *ab*
342 *initio* molecular dynamics simulations of the three systems at 300 K and examined the
343 proton transfer coordinates defined as the difference in distance between the proton (H)
344 and the two oxygen atoms (O1 and O2) that sandwich it and is commonly referred to as the
345 proton transfer coordinate (d_{O1-H}-d_{O2-H}) as shown in Fig. 4a for different types of hydrogen
346 bonds in the crystals. It is clear that the SHB in L-pyro-amm is characterised by a double-well
347 potential. The barrier associated with this proton transfer is on the order of thermal energy,
348 indicating that zero-point energy (ZPE) would make the proton transfer barrierless (*35*). An
349 examination of similar proton transfer coordinates for hydrogen bonds in L-glu and L-pyro
350 show that they are characterised by only single-well potentials.
351
352 The nature of the optical properties is sensitive to the environment in which the glutamine
353 molecules reside. It has previously been reported that charged amino acids already display
354 an absorption in the range of 250-350 nm that is significantly red shifted (*36*, *37*). The
355 origins of the low energy absorption were attributed to charge transfer excitations. The
356 simulations of these systems were performed in the gas phase, rather than considering the
357 protein environment such as shown for L-pyro-amm in Fig 2d. In comparison to the results
358 presented in Fig. 2d, data presented in Fig. 3, show that the origins of the electronic
359 transitions equally arise from a charge transfer (CT) between the highest occupied
360 molecular orbital (HOMO) on the anionic dimer, and the lowest unoccupied molecular
361 orbital (LUMO) centred on the ammonium cation when performed in the gas phase.
362 Interestingly, the correct transition energy is only predicted when the ammonium cation is

spatially near the centre of the dimer, which corresponds to the delocalisation of the negative charge and the SHB. Two generalised geometries, with the ammonium cation near the SHB (as seen in Fig. 3a) and away from the SHB (Fig. 3b), with the corresponding HOMO and LUMO orbitals are shown. The results predict a transition of 303.50 nm for dimer a. and 668.66 nm for dimer b., with dimer a. most closely resembling the chemical environment present within the crystalline material.

The results show that charge transfer is capable to lead to absorption in the far UV when investigated in the gas phase, i.e. neglecting the direct protein environment. However, including the protein environment in the molecular crystal (Fig. 2d) results instead in the excitation being a charge reorganisation involving several different molecular groups of the crystal. Indeed, by shuffling the protons along the SHBs in the ground-state, we observe an electronic response involving the entire structural units of L-pyro-amm including both the hydrogen bonded regions and the pyroglutamic acid rings when the protein environment is accounted for (Suppl. Fig.3b i-iv).

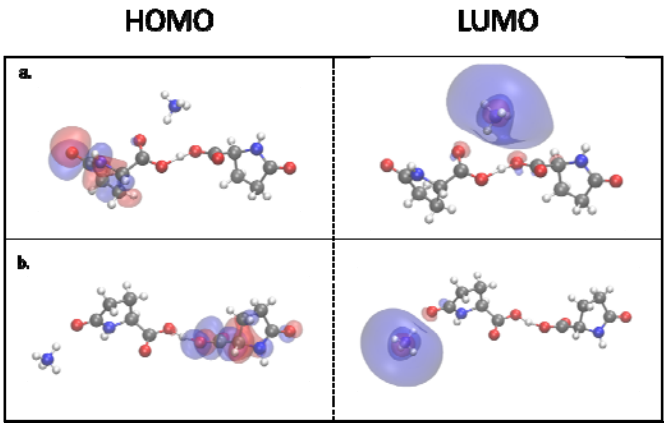

Figure 3. Comparison of the HOMO and LUMO orbitals on two L-Pyro-Amm models. L-pyro-Amm structures are presented where the ammonium cation is located directly near the hydrogen bond (a), and where the ammonium cation is located away from the hydrogen bond (b). While both models predicted charge-transfer HOMO-LUMO states, only in the case of (a) is the transition predicted to be in the vicinity of the experimentally observed peak, 303.50 nm compared to 668.66 nm for (b).

Up to this point, we have shown that the vibrations of protons along SHBs are an important part of the structural fluctuations in the ground state structure of L-pyro-amm. These calculations however, do not say anything about the nuclear relaxation upon photo-excitation which is most relevant for fluorescence. In a final set of theoretical studies, to ascertain the role of the proton transfer in the ground state, as well as to elucidate the presence of other types of vibrational modes, we performed a series of geometry optimisations on the first excited state of a cluster carved out from L-glu, L-pyro and L-pyro-amm crystals and surrounded by a continuum dielectric constant of 80.

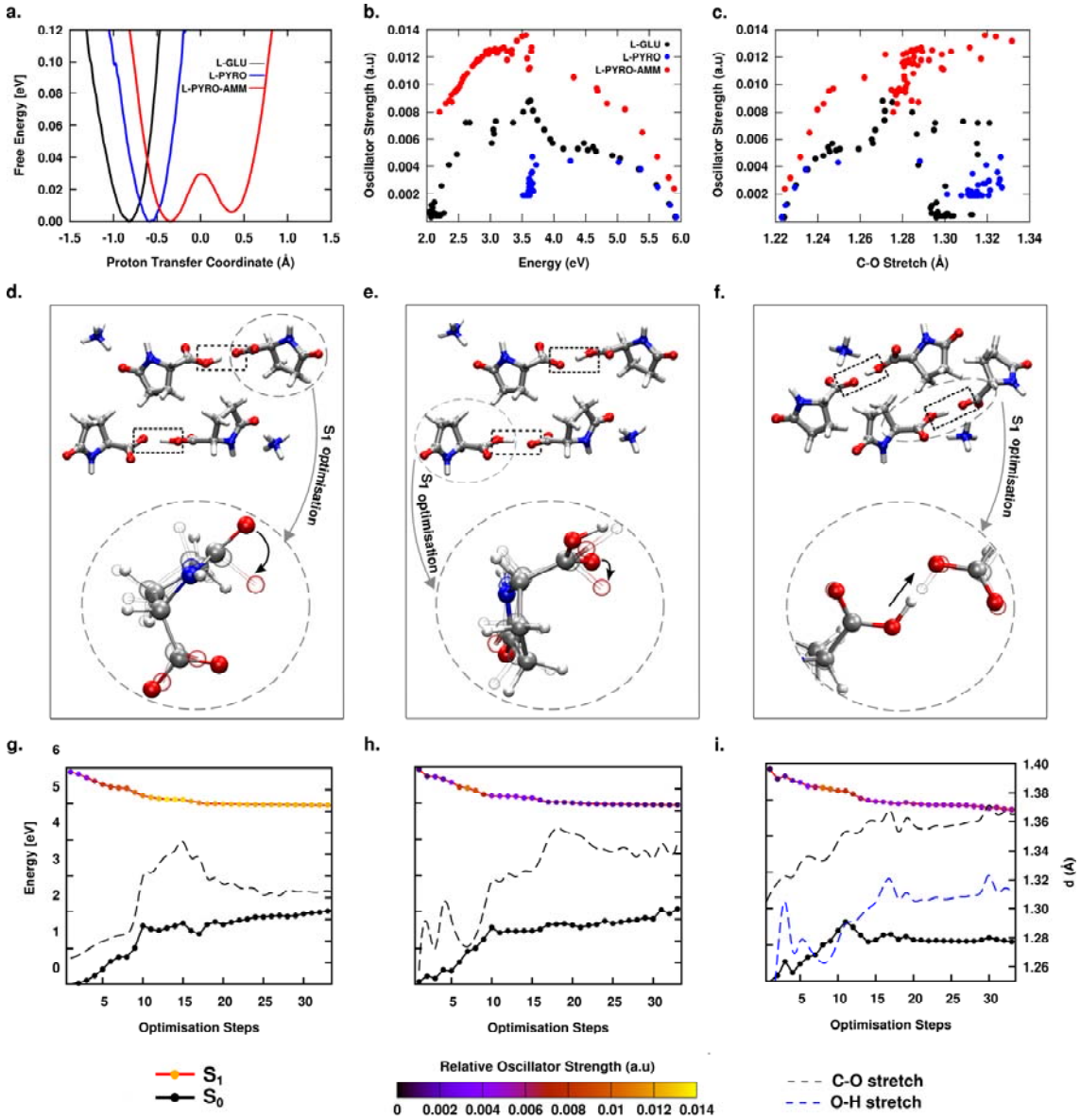

397 **Figure 4. Collective vibrations affect the emission in L-pyro-amm**

398 a) Shows the proton transfer free energy profiles along several hydrogen bonds in L-glu, L-
399 pyro and L-pyro-amm obtained from ground-state ab initio molecular dynamics simulations.
400 Note, the SHB in L-pyro-amm is characterised by a double-well potential. b) Scatter plot of
401 the oscillator strengths versus the emission energy (defined as the difference between the
402 first excited state and the ground-state) during the excited optimisations for L-glu, L-pyro
403 and L-pyro-amm. c) Scatter plot of the oscillator strengths versus the distance of the
404 carbonyl bond (C=O) that extends during the excited state optimisation in L-glu, L-pyro and
405 L-pyro-amm. d)-f) Snapshots of three different systems of L-pyro-amm that were optimised
406 on the excited state. In clusters shown in d) and e) the initial position of the proton along
407 the SHB has been changed, and in f) the ammonium ion has been placed closer to the SHB
408 region. The bottom panel of d), e) and f) show zoomed in plots of the main regions of the
409 cluster (circled in the top panels) that undergo significant changes. g)-i) Ground and excited
410 state energies are plotted as a function of the excited state optimisation for the three
411 systems shown in panels d-f). The curves on the excited state are colour-coded with the
412 oscillator strengths. S_0 and S_1 refer to the ground and excited state energies, respectively.
413 The right-side of the y-axis corresponds to C=O bond lengths (dashed black lines) for g) and
414 h). In panel i), where there is a proton transfer on the excited state, the dashed blue lines
415 correspond to the O-H distance along the SHB on the same distance scale.

416

417 Fig. 4b shows a scatter plot of the difference between the first excited state and ground-
418 state energies and the corresponding oscillator strengths. The scatter plots were obtained
419 over the course of the excited state optimisation. We observe that the L-pyro-amm system
420 is characterised by the largest oscillator strengths compared to L-glu or L-pyro. One of the
421 major structural changes that occurs upon excitation is an increase in the C=O bond length
422 similar to observations in previous studies (*38–40*). Fig. 4c shows the oscillator strengths as
423 a function of the C=O bond, that increases in length by about 0.1 Angstroms.

424

425 Although all three glutamine-related structures display similar trends on the excited state,
426 what makes L-pyro-amm unique is the presence of the SHB. Fig. 4b and c show that L-pyro-
427 amm displays the largest oscillator strength peaking at approximately 3.5eV consistent with
428 our experimental findings. Although L-glu also has a peak at around 3.5 eV it is much weaker

than the one of L-pyro-amm. We thus decided to focus on a series of excited state optimisations for various clusters of L-pyro-amm. In particular, we focused on the proton transfer in the ground state as seen in the double-well potential and on the proximity of the ammonium ion to the short hydrogen bond region, all shown to play an important role in the optical properties of L-pyro-amm so far. We thus constructed three clusters with different initial conditions, which are shown in the top panels of Fig. 4d-f. The clusters shown in Fig. 4d and 4e differ in the initial positions of the protons along the SHB. As seen in Fig. 4a, the ground-state simulations of L-pyro-amm present a double-well potential in the finite temperature simulations. We thus moved the proton along one of the SHBs, constrained the geometry in the ground-state which yielded the cluster shown in Fig. 4e. In Fig. 4f, the ammonium ion is placed closer to the SHB region.

The circled regions in Fig. 4d-f highlight the main regions, where the nuclear degrees of freedom respond in the excited state. The bottom panels show a zoomed in image of the changes that occur upon relaxation, for which the solid and transparent structures correspond to geometries obtained before and after the relaxation on the excited state, respectively. The bottom panel of Fig. 4d illustrates that the change involves the C=O stretch and deplanarisation of the peptide dihedral angle of the ring. The corresponding evolution of the first excited state and ground state energies as a function of optimisation is shown in Fig. 4g. The relaxation on the excited state narrows the energy difference between the ground and excited state to approximately 3.5eV which is consistent with the experiments.

The top panels of Fig. 4e and f involve two other initial conditions for which the proton vibrations and the proximity of the ammonium ion to the SHB are altered. We see in Fig. 4h and i that the magnitude of the oscillator strength of L-pyro-amm in the excited state is sensitive to these new initial conditions. Transferring the protons on the ground-state (see dotted black rectangles in Fig. 4d-f), significantly changes the oscillator strengths as seen in the comparison between Fig. 4g-i, across the entire relaxation process in the first excited state while still maintaining the C=O stretch and deplanarisation as seen in the bottom panel of Fig. 3e. In the case of Fig. 4f, besides the reorganisation involving the C=O stretch, we also observe a proton transfer along the SHB. This is seen in Fig. 4i, which shows the O-H stretch (dashed-blue curve) along the SHB during the optimisation which increases from

461 1.26 to 1.32 Angstroms. The zoomed in plot in the bottom panel of Fig. 4f shows this subtle
462 change in the proton transfer coordinate. Thus, the evolution of the excited state in L-pyro-
463 amm into the region displaying visible fluorescence appears to involve a collective
464 reorganisation of various vibrational modes forming the hydrogen bond network with the
465 SHB playing a particular role, as it leads to the brightest structure, also confirmed
466 experimentally. These findings are also consistent with some recent theoretical work
467 showing the importance of proton transfer in self-assembled peptides made of aromatic
468 phenyl-alanine amino acids (*41*). However, the latter structure features an aromatic amino
469 acid, whereas we observe similar optical properties in non-aromatic structures.
470
471 **Conclusions**
472
473 The experimental and theoretical findings presented here, elucidate a rather complex
474 molecular mechanism associated with the non-aromatic intrinsic fluorescence in protein-
475 like structures. In the case of L-glutamine, a chemical reaction creates a newly formed
476 structure involving a cyclised pyroglutamic acid ring. This new structure features absorption
477 in the UV and emission in the visible range very similar to the chemically distinct amyloid
478 fibrils (*4*, *5*, *11*, *12*, *41*–*43*).
479
480 The structural chromophore responsible for the optical properties in this new protein-
481 related structure arises from a hydrogen bond network characterised by specific vibrational
482 fluctuations on the excited state. The presence of strong hydrogen bonds along which
483 proton transfer occurs and secondly, specific ionic interactions in close proximity, such as
484 involving the ammonium ion, affect the optical properties. Although the fluorescence
485 observed in these systems is much weaker than those compared to conventional
486 fluorophores, the physical and chemical properties of the hydrogen bond network reported
487 here maybe a generic feature across many other peptide structures.
488
489 In summary, we show here that there are several vibrational modes in biological structures
490 that contribute to fluorescence properties as shown by excited state simulations and
491 confirmed experimentally. We further show that the protein environment strongly
492 contributes to the optical activity of the protein like structure and that the SHB significantly

enhances the fluorescence signal detected, potentially by inhibiting a conical intersection in the excited state as discussed previously (*5*). Interestingly, SHBs have recently been observed in different biological systems which have long been associated with either intrinsic fluorescence, such as NADP/NAD (*44*), FAD/FMN (*45*), the light-sensing chromophore in photoactive yellow protein (*46*), or in the active site of many enzymes, such as hydrolases and oxidoreductases (*47*, *48*), many of which consist of a highly complex H-bond structure similar to amyloid proteins. Our findings may thus further the design of novel optically active biomaterial for applications in optical sensing or the design of novel biocompatible catalysts.

Author Information

Corresponding Authors

Ali A. Hassanali, ahassana@ictp.it

Gabriele S. Kaminski Schierle, gsk20@cam.ac.uk

Author Contributions

*A.D.S and M.N.Q contributed equally. A.D.S, prepared samples for all experimental data. P.J.W. performed SEM experiments. A.D.B and M.T.R performed XRD measurements and analysed data. M.T.R. performed THz experiments and DFT-THz calculations and analysed data. A.D.S. performed excitation and emission measurements and analysed data. A.D.S and S.T.J. performed absorption measurements and analysed data. M.T.R and E.M.K performed TD-DFT cluster calculations. M.N.Q, E.P, L.G, R.G and A.H performed AIMD, Periodic TD-DFT Excited State Calculations and Periodic Structure Geometry Optimisation calculations. A.D.S, M.N.Q, M.T.R, S.T.J, L.G, J.A.Z, D.C, A.H and G.S.K.S contributed to manuscript writing. All authors have given approval to the final version of the manuscript.

Notes

The authors declare no competing financial interest.

Acknowledgments

G.S.K.S. acknowledges funding from the Wellcome Trust, the UK Medical Research Council (MRC), Alzheimer Research UK (ARUK), and Infinitus China Ltd. A.D.S. acknowledge

Alzheimer Research UK the British Biophysical Society (BSS) for travel grants. P.J.W acknowledges EPSRC funding (EP/L016087/1).

Supplementary data

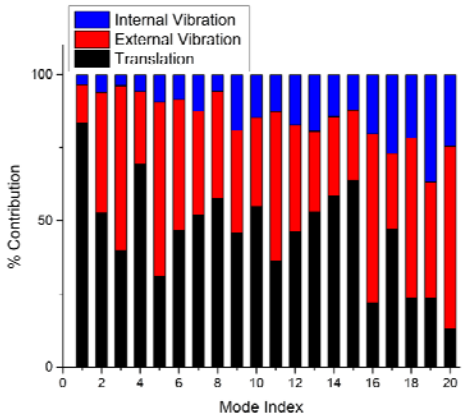

Mode Number	Frequency (THz)	Intensity (km mol^{A}-1)	Assignment
1	0.955	0.22	Antisymmetric translation in b
2	1.215	0.71	Coupled translation in a and rotation about bc
3	1.325	1.52	external rotation about b
4	1.450	0.36	Asymmetric translation in c
5	1.554	4.37	External rotation about a
6	1.676	1.76	Translation in a and external asymmetric rotation about H-bond coordinate
7	1.805	2.28	External asymmetric rotation of dimer pairs
8	1.929	2.11	External symmetric rotation of dimer pairs
9	1.950	1.28	Asymmetric rotation about h-bond coordinate, ammonium translational motion
10	2.113	3.53	Translation and rotation (breathing) around ammonium cation
11	2.208	2.5	Symmetric external rotation of entire formula units
12	2.404	2.37	In phase external rotation perpendicular to h-bond coordinate
13	2.502	0.45	Out of phase external rotatalon perpendicular to h-bond coordinate
14	2.564	0.73	External out of phase rotatalon of h-bonded chains about b
15	2.565	8.91	Out of phase external rotation of individual pyroglutamic molecules with translation of ammonium cation
16	2.654	18.09	External vibration coupled with torsion of the COOH group
17	2.679	0.29	External rotation and torsion of pyroglutamic ring
18	2.776	4.94	External rotation and torsion of ring and carboxyl group
19	2.988	2.68	External rotatalon and translation of ammonium

Supplementary Figure 1. Full spectral assignment of THz data.

The top chart shows the contribution to each IR-active mode including external translations and hindered rotations, and internal vibrational motions (i.e. torsions), while the bottom table lists the detailed assignment for each mode.

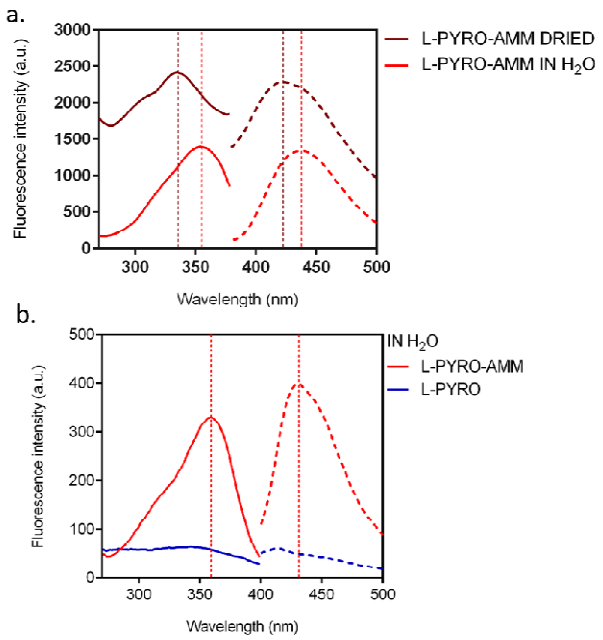

Supplementary Figure 2. L-pyro-amm has blue shifted fluorescence when dried and displays higher fluorescence intensity than L-pyro.

(a)The excitation peak of L-pyro-amm when dried (solid dark red line) is blue shifted with a peak maximum ~ 340 nm compared to L-pyro-amm in H_2O (solid red line) which has a peak maximum ~ 360 nm. The emission peak of L-pyro-amm when dried (dashed dark red line) is also blue shifted, with a peak maximum ~ 420 nm, compared to L-pyro-amm in H_2O (dashed red line) with a peak maximum ~ 430 nm. (b) 1 M L-glu and 1 M L-pyro (blue) were incubated in H_2O for 8 days at 65°C. After 9 days, the L-glu had converted into the L-pyro-amm structure (red). L-pyro-amm has a clear excitation peak maximum at ~360 nm and emission peak maximum at ~ 430 nm, while L-pyro (blue), although not completely dark, has no clear excitation or emission peak.

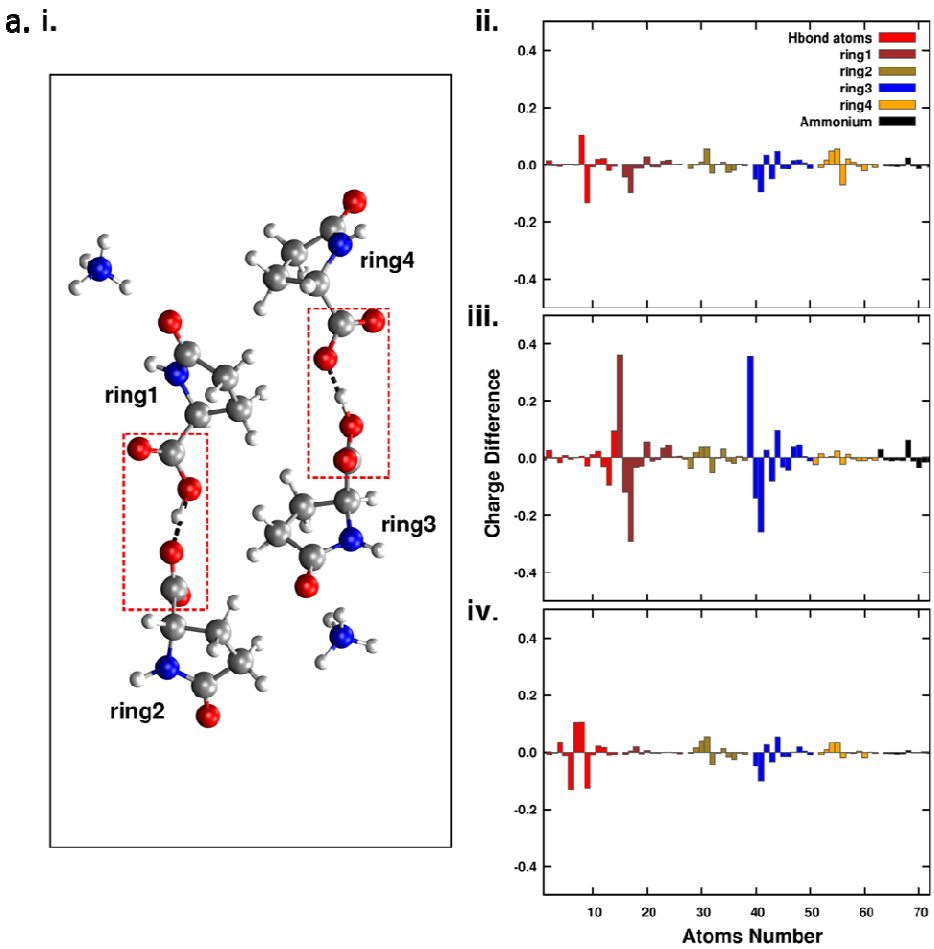

Supplementary Figure 3. The optical properties of L-pyro-amm are sensitive to the environment and involves the electronic response of the entire structure.

(a)(i) L-pyro-amm cluster used to examine the sensitivity of the optical response on different parts of the cluster upon moving different protons. (ii) Charge differences between the ground and excited state are computed using restrained electrostatic potential atomic partial charges (RESP) for the cluster shown in i). Note, the electronic response involves all the atoms of the cluster. (iii) The two protons in the rectangle regions are displaced to be in the centre of the hydrogen bond and the charge differences are then computed. As illustrated, the proton displacement leads to a larger change in magnitude of the charges. (iv) The charge differences are computed for another nuclear configuration for which the protons are kept fixed but the O—O distance is increased from 2.45 to 3.2 Angstroms. The charge differences obtained here are quite similar to the original condition shown in (ii).

570 **References:**

571 1. A. Shukla, S. Mukherjee, S. Sharma, V. Agrawal, K. V. R. Kishan, P. Guptasarma, A
572 novel UV laser-induced visible blue radiation from protein crystals and aggregates:
573 Scattering artifacts or fluorescence transitions of peptide electrons delocalized
574 through hydrogen bonding? *Arch. Biochem. Biophys.* **428**, 144–153 (2004).
575 2. G. Rosenman, N. Amdursky, M. Molotskii, D. Aronov, L. Adler-Abramovich, E. Gazit,
576 Blue luminescence based on quantum confinement at peptide nanotubes. *Nano Lett.*
577 **9**, 3111–3115 (2009).
578 3. F. T. Chan, D. Pinotsi, G. S. K. Schierle, C. F. Kaminski, in *Bio-nanoimaging: Protein*
579 *Misfolding and Aggregation* (Elsevier, 2013;
580 http://linkinghub.elsevier.com/retrieve/pii/B9780123944313000134), pp. 147–155.
581 4. F. T. S. Chan, G. S. Kaminski Schierle, J. R. Kumita, C. W. Bertoncini, C. M. Dobson, C. F.
582 Kaminski, C. V Robinson, C. M. Dobson, J. Beard, P. Das, K. Jansen, M. DeLucia, W.-L.
583 Lin, G. Dolios, R. Wang, C. B. Eckman, D. W. Dickson, M. Hutton, J. Hardy, T. Golde,
584 Protein amyloids develop an intrinsic fluorescence signature during aggregation.
585 *Analyst*. **138**, 2156 (2013).
586 5. D. Pinotsi, L. Grisanti, P. Mahou, R. Gebauer, C. F. Kaminski, A. Hassanali, G. S.
587 Kaminski Schierle, Proton Transfer and Structure-Specific Fluorescence in Hydrogen
588 Bond-Rich Protein Structures. *J. Am. Chem. Soc.* **138**, 3046–3057 (2016).
589 6. J. Pansieri, V. Josserand, S. J. Lee, A. Rongier, D. Imbert, M. M. Sallanon, E. Kövari, T.
590 G. Dane, C. Vendrely, O. Chaix-Pluchery, M. Guidetti, J. Vollaire, A. Fertin, Y. Usson, P.
591 Rannou, J. L. Coll, C. Marquette, V. Forge, Ultraviolet–visible–near-infrared optical
592 properties of amyloid fibrils shed light on amyloidogenesis. *Nat. Photonics*. **13**, 473–
593 479 (2019).
594 7. L. Adler-Abramovich, E. Gazit, Correction: The physical properties of supramolecular
595 peptide assemblies: From building block association to technological applications.
596 *Chem. Soc. Rev.* **43**, 7236–7236 (2014).
597 8. L. Adler-Abramovich, M. Reches, V. L. Sedman, S. Allen, S. J. B. Tendler, E. Gazit,
598 Thermal and chemical stability of diphenylalanine peptide nanotubes: Implications for
599 nanotechnological applications. *Langmuir*. **22**, 1313–1320 (2006).
600 9. K. Tao, P. Makam, R. Aizen, E. Gazit, Self-assembling peptide semiconductors. *Science*
601 *(80-.).* **358** (2017), p. eaam9756.

602 10. J. M. Andresen, J. Gayán, L. Djoussé, S. Roberts, D. Brocklebank, S. S. Cherny, L. R.
603 Cardon, J. F. Gusella, M. E. Macdonald, R. H. Myers, D. E. Housman, N. S. Wexler, J.
604 Lorimer, J. Porter, F. Gomez, C. Moskowitz, K. P. Gerstenhaber, E. Shackell, K. Marder,
605 G. Penchaszadeh, S. A. Roberts, A. Brickman, D. Brocklebank, J. Gray, S. R. Dlouhy, S.
606 Wiktorski, M. E. Hodes, P. M. Conneally, J. B. Penney, J. F. Gusella, J. H. Cha, M.
607 Irizarry, D. Rosas, S. Hersch, Z. Hollingsworth, A. B. Young, D. E. Housman, M. M. de
608 Young, E. Bonilla, T. Stillings, A. Negrette, S. R. Snodgrass, M. D. Martinez-Jaurrieta,
609 M. A. Ramos-Arroyoh, J. Bickham, J. S. Ramos, F. Marshall, I. Shoulson, G. J. Rey, A.
610 Feigin, N. Arnheim, A. Acevedo-Cruz, L. Acosta, J. Alvir, K. Fischbeck, L. M. Thompson,
611 A. Young, L. Dure, C. J. O'Brien, J. Paulsen, S. P. Moran, D. Krch, P. Hogarth, D. S.
612 Higgins, B. Landwehrmeyer, M. R. Hayden, E. W. Almqvist, R. R. Brinkman, O.
613 Suchowersky, A. Durr, C. C. Dodé, F. Squitieri, P. J. Morrison, M. Nance, C. A. Ross, R.
614 L. Margolis, A. Rosenblatt, G. T. Estrella, D. M. Cabrero, R. J. A. Trent, E. McCusker, A.
615 Novelletto, M. Frontali, J. S. Paulsen, R. Jones, A. Zanko, T. Ashizawa, A. Lazzarini, J. L.
616 Li, V. C. Wheeler, A. L. Russ, G. Xu, J. S. Mysore, T. Gillis, M. Hakky, L. A. Cupples, M.
617 Saint-Hilaire, S. M. Hersch, The relationship between CAG repeat length and age of
618 onset differs for Huntington's disease patients with juvenile onset or adult onset.
619 *Ann. Hum. Genet.* **71**, 295–301 (2007).
620 11. D. Pinotsi, A. K. Buell, C. M. Dobson, G. S. Kaminski Schierle, C. F. Kaminski, A Label-
621 Free, Quantitative Assay of Amyloid Fibril Growth Based on Intrinsic Fluorescence.
622 *ChemBioChem*. **14**, 846–850 (2013).
623 12. T. N. Tikhonova, N. R. Rovnyagina, A. Y. Zherebker, N. N. Sluchanko, A. A. Rubekina, A.
624 S. Orekhov, E. N. Nikolaev, V. V. Fadeev, V. N. Uversky, E. A. Shirshin, Dissection of the
625 deep-blue autofluorescence changes accompanying amyloid fibrillation. *Arch.*
626 *Biochem. Biophys.* **651**, 13–20 (2018).
627 13. H. Mori, K. Takio, M. Ogawara, D. J. Selkoe, Mass spectrometry of purified amyloid β
628 protein in Alzheimer's disease. *J. Biol. Chem.* **267**, 17082–17086 (1992).
629 14. M. Fändrich, C. M. Dobson, The behaviour of polyamino acids reveals an inverse side
630 chain effect in amyloid structure formation. *EMBO J.* **21**, 5682–90 (2002).
631 15. R. Dovesi, A. Erba, R. Orlando, C. M. Zicovich-Wilson, B. Civalleri, L. Maschio, M. Rérat,
632 S. Casassa, J. Baima, S. Salustro, B. Kirtman, Quantum-mechanical condensed matter
633 simulations with CRYSTAL. *Wiley Interdiscip. Rev. Comput. Mol. Sci.* **8**, e1360 (2018).

16. P. Giannozzi, O. Andreussi, T. Brumme, O. Bunau, M. Buongiorno Nardelli, M. Calandra, R. Car, C. Cavazzoni, D. Ceresoli, M. Cococcioni, N. Colonna, I. Carnimeo, A. Dal Corso, S. De Gironcoli, P. Delugas, R. A. Distasio, A. Ferretti, A. Floris, G. Fratesi, G. Fugallo, R. Gebauer, U. Gerstmann, F. Giustino, T. Gorni, J. Jia, M. Kawamura, H. Y. Ko, A. Kokalj, E. Kücükbenli, M. Lazzeri, M. Marsili, N. Marzari, F. Mauri, N. L. Nguyen, H. V. Nguyen, A. Otero-De-La-Roza, L. Paulatto, S. Poncé, D. Rocca, R. Sabatini, B. Santra, M. Schlipf, A. P. Seitsonen, A. Smogunov, I. Timrov, T. Thonhauser, P. Umari, N. Vast, X. Wu, S. Baroni, Advanced capabilities for materials modelling with Quantum ESPRESSO. *J. Phys. Condens. Matter*. **29** (2017), doi:10.1088/1361-648X/aa8f79.

17. M. T. Ruggiero, J. Gooch, J. Zubieta, T. M. Korter, Evaluation of Range-Corrected Density Functionals for the Simulation of Pyridinium-Containing Molecular Crystals. *J. Phys. Chem. A*. **120**, 939–947 (2016).

18. J. Da Chai, M. Head-Gordon, Long-range corrected hybrid density functionals with damped atom-atom dispersion corrections. *Phys. Chem. Chem. Phys.* **10**, 6615–6620 (2008).

19. D. Rocca, R. Gebauer, Y. Saad, S. Baroni, Turbo charging time-dependent density-functional theory with Lanczos chains. *J. Chem. Phys.* **128** (2008), doi:10.1063/1.2899649.

20. N. Troullier, J. L. Martins, Efficient pseudopotentials for plane-wave calculations. *Phys. Rev. B*. **43**, 1993–2006 (1991).

21. A. D. Becke, Density-functional thermochemistry. III. The role of exact exchange. *J. Chem. Phys.* **98**, 5648–5652 (1993).

22. J. D. Head, M. C. Zerner, A Broyden-Fletcher-Goldfarb-Shanno optimization procedure for molecular geometries. *Chem. Phys. Lett.* **122**, 264–270 (1985).

23. J. VandeVondele, M. Krack, F. Mohamed, M. Parrinello, T. Chassaing, J. Hutter, Quickstep: Fast and accurate density functional calculations using a mixed Gaussian and plane waves approach. *Comput. Phys. Commun.* **167**, 103–128 (2005).

24. S. Goedecker, M. Teter, Separable dual-space Gaussian pseudopotentials. *Phys. Rev. B - Condens. Matter Mater. Phys.* **54**, 1703–1710 (1996).

25. A. D. Becke, Density-functional exchange-energy approximation with correct asymptotic behavior. *Phys. Rev. A*. **38**, 3098–3100 (1988).

26. S. Grimme, J. Antony, S. Ehrlich, H. Krieg, A consistent and accurate *ab initio*

666 parametrization of density functional dispersion correction (DFT-D) for the 94
667 elements H-Pu. *J. Chem. Phys.* **132**, 154104 (2010).
668 27. G. Bussi, D. Donadio, M. Parrinello, Canonical sampling through velocity rescaling. *J.*
669 *Chem. Phys.* **126** (2007), doi:10.1063/1.2408420.
670 28. T. Yanai, D. P. Tew, N. C. Handy, A new hybrid exchange-correlation functional using
671 the Coulomb-attenuating method (CAM-B3LYP). *Chem. Phys. Lett.* **393**, 51–57 (2004).
672 29. K. Jong, Y. Taghipour Azar, L. Grisanti, A. D. Stephens, S. T. E. Jones, D. Credgington, G.
673 S. Kaminski Schierle, A. A. Hassanali, Low Energy Optical Excitations as an Indicator of
674 Structural Changes Initiated at the Termini of Amyloid Protein. *Phys. Chem. Chem.*
675 *Phys.* (2019), doi:10.1039/c9cp04648h.
676 30. L. Grisanti, D. Pinotsi, R. Gebauer, G. S. Kaminski Schierle, A. A. Hassanali, A
677 computational study on how structure influences the optical properties in model
678 crystal structures of amyloid fibrils. *Phys. Chem. Chem. Phys.* **19**, 4030–4040 (2017).
679 31. E. P. J. Parrott, J. A. Zeitler, Terahertz time-domain and low-frequency Raman
680 spectroscopy of organic materials. *Appl. Spectrosc.* **69**, 1–25 (2015).
681 32. Y. K. Law, A. A. Hassanali, Role of Quantum Vibrations on the Structural, Electronic,
682 and Optical Properties of 9-Methylguanine. *J. Phys. Chem. A.* **119**, 10816–10827
683 (2015).
684 33. S. Sappati, A. Hassanali, R. Gebauer, P. Ghosh, Nuclear quantum effects in a
685 HIV/cancer inhibitor: The case of ellipticine. *J. Chem. Phys.* **145** (2016),
686 doi:10.1063/1.4968046.
687 34. Y. K. Law, A. A. Hassanali, The importance of nuclear quantum effects in spectral line
688 broadening of optical spectra and electrostatic properties in aromatic chromophores.
689 *J. Chem. Phys.* **148** (2018), doi:10.1063/1.5005056.
690 35. D. Marx, Erratum: Proton transfer 200 years after von grotthuss: Insights from Ab
691 initio simulations (ChemPhysChem (2006) 7 (1848-1810)). *ChemPhysChem*. **8**, 209–
692 210 (2007).
693 36. S. Prasad, I. Mandal, S. Singh, A. Paul, B. Mandal, R. Venkatramani, R. Swaminathan,
694 Near UV-Visible electronic absorption originating from charged amino acids in a
695 monomeric protein. *Chem. Sci.* **8**, 5416–5433 (2017).
696 37. I. Mandal, S. Paul, R. Venkatramani, Optical backbone-sidechain charge transfer
697 transitions in proteins sensitive to secondary structure and modifications. *Faraday*

Discuss. **207**, 115–135 (2018).

38. M. Mališ, Y. Loquais, E. Gloaguen, H. S. Biswal, F. Piuzzi, B. Tardivel, V. Brenner, M. Broquier, C. Jouvet, M. Mons, N. D. S. Došlić, I. Ljubić, Unraveling the mechanisms of nonradiative deactivation in model peptides following photoexcitation of a phenylalanine residue. *J. Am. Chem. Soc.* **134**, 20340–20351 (2012).

39. B. P. Fingerhut, K. E. Dorfman, S. Mukamel, Monitoring nonadiabatic dynamics of the RNA base uracil by UV pump-IR probe spectroscopy. *J. Phys. Chem. Lett.* **4**, 1933–1942 (2013).

40. M. Sapunar, T. Ayari, N. Došlić, Comparative study of the photodynamics of malonaldehyde and acetylacetone. *Chem. Phys.* **515**, 622–627 (2018).

41. S. K. Joseph, N. Kuritz, E. Yahel, N. Lapshina, G. Rosenman, A. Natan, Proton-Transfer-Induced Fluorescence in Self-Assembled Short Peptides. *J. Phys. Chem. A.* **123**, 1758–1765 (2019).

42. A. Handelman, N. Kuritz, A. Natan, G. Rosenman, Reconstructive Phase Transition in Ultrashort Peptide Nanostructures and Induced Visible Photoluminescence. *Langmuir*. **32** (2016), pp. 2847–2862.

43. L. L. Del Mercato, P. P. Pompa, G. Maruccio, A. Della Torre, S. Sabella, A. M. Tamburro, R. Cingolani, R. Rinaldi, Charge transport and intrinsic fluorescence in amyloid-like fibrils. *Proc Natl Acad Sci U S A.* **104**, 18019–18024 (2007).

44. A. Stavrinides, E. C. Tatsis, L. Caputi, E. Foureau, C. E. M. Stevenson, D. M. Lawson, V. Courdavault, S. E. O'Connor, Structural investigation of heteroyohimbine alkaloid synthesis reveals active site elements that control stereoselectivity. *Nat. Commun.* **7** (2016), doi:10.1038/ncomms12116.

45. F. Forneris, D. P. H. M. Heuts, M. Delvecchio, S. Rovida, M. W. Fraaije, A. Mattevi, Structural analysis of the catalytic mechanism and stereoselectivity in Streptomyces coelicolor alditol oxidase. *Biochemistry*. **47**, 978–985 (2008).

46. S. Yamaguchi, H. Kamikubo, K. Kurihara, R. Kuroki, N. Niimura, N. Shimizu, Y. Yamazaki, M. Kataoka, Low-barrier hydrogen bond in photoactive yellow protein. *Proc. Natl. Acad. Sci. U. S. A.* **106**, 440–444 (2009).

47. W. W. Cleland, P. A. Frey, J. A. Gerlt, The low barrier hydrogen bond in enzymatic catalysis. *J. Biol. Chem.* **273** (1998), pp. 25529–25532.

48. S. Zhou, L. Wang, Unraveling the structural and chemical features of biological short

730 hydrogen bonds. *Chem. Sci.* **10**, 7734–7745 (2019).

731